Article

Journal of Vibration and Control
1–21

DOI: 10.1177/1077546316681685
jvc.sagepub.com
SAGE

A viscoelastic Timoshenko shaft finite element for dynamic analysis of rotors

Smitadhi Ganguly[1], A Nandi[2] and S Neogy[2]

Abstract

A new shaft element is proposed for viscoelastic rotors in a spinning frame considering the shear deformation in addition to bending deformation. The Maxwell–Wiechert model is considered here to replicate linear viscoelastic behavior. This model considers additional internal damping displacement variables between elastic and viscous elements and the stress depends not only on the elastic strain and elastic strain rate, but also on additional strains and their rates corresponding to the damping variables. The present work assumes that these additional strains can be derived from continuous fictitious displacement variables, which in turn are interpolated from their nodal values using the Timoshenko beam shape functions. Therefore, in addition to the standard degrees of freedom for a three-dimensional shaft, extra degrees of freedom are defined at the nodes. The finite element matrices are assembled in state space. The time domain equations are then used for stability analysis and computation of response to a unit step load and an unbalance.

Keywords

Viscoelastic rotor, Timoshenko beam, state space, stability, time response

1. Introduction

It is a well-established fact that for stress analysis of linear viscoelastic structures involving linear viscoelastic materials, Laplace transform of the stress–strain relations is considered to transform the problem in the Laplace domain (Williams, 1964). The solution of this problem can be transformed back to the time domain to obtain the solution of the original problem. Therefore, for viscoelastic components subjected to harmonic loading, a frequency-domain analysis is most suitable. Here one directly uses the frequency-dependent storage modulus and loss coefficient in the material model. However, for other type of loadings, a time-dependent viscoelastic material model is essential, particularly in the context of finite element analysis.

The Maxwell–Wiechert model has been used by many to model linear viscoelasticity. It offers the advantage of being suitable for both frequency domain and time domain formulations. The GHM method (Golla and Hughes, 1985) uses a modified Maxwell–Wiechert model which is especially suitable for using with finite element analysis. Physically, this method associates small masses with the additional over damped oscillators constituting the parallel Maxwell branches. The inertia, stiffness, and damping of the oscillators can be determined from experimental data (McTavish and Hughes, 1993). In recent times, Adhikari has studied similar energy dissipation phenomena in structures in great detail and has used the term nonviscous damping (Adhikari, 2001, 2002; Adhikari and Wagner, 2003; Wagner and Adhikari, 2003; Adhikari, 2005, 2008). De Lima et al. (2006) has developed sensitivity analysis of viscoelastic plates treated with constraining damping layers using a finite element method with complex modulus approach.

Lesieutre and Mingori (1990) have developed a novel method of modelling frequency dependent damping in time domain by introducing augmenting thermodynamic fields (ATF) which interact with mechanical displacement fields. A similar time domain model of linear

[1]Department of Mechanical Engineering, Hooghly Engineering and Technology College, India
[2]Department of Mechanical Engineering, Jadavpur University, Kolkata, India

Received: 18 October 2016; accepted: 4 November 2016

Corresponding author:
Smitadhi Ganguly, Department of Mechanical Engineering, Hooghly Engineering and Technology College, Hooghly 712103, West Bengal, India.
Email: smitadhi@hetc.ac.in

viscoelasticity, where anelastic displacement fields (ADF) are added to elastic displacements, has also been presented by Lesieutre and coworkers (Lesieutre and Bianchini, 1995; Lesieutre et al, 1996) to take care of strains which were not instantaneous. Rusovici (1999) has employed these models in analysis of shock wave propagation in viscoelastic structures. Roy et al. (2009) have used ATF/ADF models in dynamic analysis of a layered viscoelastic beam. The ATF model has been utilized in conjunction with finite elements by Friswell et al. (2010) for analysis of rotors made of viscoelastic materials. They have used the Euler–Bernoulli shaft element with an internal variable formulation and presented stability analysis of slender rotors.

Viscoelastic rotors and supports have also been investigated in great detail. Kliem (1987) has discussed the stability of viscoelastic rotors using a two-parameter as well as a three-parameter solid model. Sinha (1989) has studied the stability of viscoelastic rotor–disk models under dynamic axial loads. Free and forced response of a spinning viscoelastic Rayleigh shaft has been computed using a three-parameter model by Sturla and Argento (1996). Shabaneh and Zu (2000a, 2000b) have performed dynamic analysis of a rotating shaft–disk system on linear elastic springs mounted on viscoelastic suspension. Bavastri et al. (2008) have analyzed a rotor simply supported on viscoelastic bearings using a four parameter fractional derivative model. Genta and coworkers have applied the concept of nonviscous damping in analyzing rotors (Genta et al., 1996; Genta and Amati, 2010). Kang et al. (2011) have investigated the dynamic behavior of a gear–rotor system with viscoelastic supports. Roy et al. (2012) have studied the dynamic behavior of a multilayered viscoelastic rotor–shaft system using beam elements.

The Timoshenko shaft element is frequently used in rotor dynamics for modeling thick shafts (Nelson, 1980; Lalanne and Ferraris, 1998). It is basically a Timoshenko beam element with appropriate gyroscopic or Coriolis terms. In recent years it has been used extensively to model rotating shafts. Hong and Park (1999) have proposed a new method to obtain exact solutions for multi-stepped rotor bearing systems, deriving an exact dynamic beam element matrix in Laplace domain for a Timoshenko shaft. A few of the papers cited above (Shabaneh and Zu, 2000a, 2000b; Bavastri et al., 2008) have utilized the Timoshenko beam theory to model rotor dynamic systems on viscoelastic supports. Xiong et al. (2003) have presented a new dynamic milling model of a rotating spindle using a Timoshenko shaft element. Cavalini and coworkers have carried out finite element simulation of rotors for checking a vibration control technique (Cavalini et al., 2011) as well as model updating (Cavalini et al., 2015) using the Timoshenko shaft element. Morais et al. (2012) have used the Timoshenko beam theory to model rotors in a numerical study on controlling of dynamic behavior through electromagnetic actuators. Dakel et al. (2014) have used the Timoshenko beam theory in studying the behavior of rotors mounted on hydrodynamic journal bearings subjected to rigid support movement. Lara-Molina et al. (2015) have used fuzzy finite element and fuzzy stochastic finite element methods to analyze the dynamics of rotors under uncertain parameters.

To the best of the knowledge and belief of the authors, a viscoelastic Timoshenko shaft finite element has not been reported previously. The present work makes a humble attempt to incorporate the Maxwell–Wiechert model into the finite element analysis of rotors using the Timoshenko shaft element. The resulting finite element model is then used to obtain both frequency response, stability analysis and time response (transient analysis) of simply supported shaft–disk systems made up of viscoelastic material.

The viscoelastic material is assumed to be incompressible and the necessary constitutive relations are imposed in the Laplace (frequency) domain. Unlike the GHM approach, the proposed method does not require elimination of the rigid body modes. The rigid body modes are automatically removed. The finite element formulation is coded in MATLAB. For transient response, the ODE suite available in MATLAB is used.

Two commonly used viscoelastic materials: ABS (acrylonitrile butadiene styrene) and PPC (polypropylene carbonate) are used for finite element analysis. The storage modulus and loss coefficient for the above-mentioned viscoelastic materials are obtained from experimental tests in a dynamics mechanical analyzer.

2. Analysis

2.1. Timoshenko beam

The elastic theory of a beam taking into account the deflection due to shear besides that due to bending, has been formulated by Timoshenko (Timoshenko, 1940). The total deformation is a summation of two parts: deformation due to bending and deformation due to direct shear. The theory specially becomes important when the transverse dimensions of the beam are not negligible compared to its axial length (Bazoune and Khulief, 2003), a condition determined by the slenderness ratio – a dimensionless quantity.

2.1.1. Stress–strain relations in an elastic Timoshenko beam. The Timoshenko beam element is a three-dimensional (3D) beam finite element which considers shear deformation. Here, the Timoshenko beam element has two perpendicular planes of bending, namely the x–y and x–z planes, assuming the x-axis to be along the

beam axis. Unlike the Euler–Bernoulli beam, where the formulation requires only modulus of elasticity (E), the Timoshenko beam calls for two material elastic constants: modulus of elasticity (E) and the shear modulus (G). The strain energy of a beam due to shear stress τ_{xy} (with corresponding strain γ_{xy}) in the x–y plane is given by

$$\begin{aligned} U_s &= \frac{1}{2}\int_V \gamma_{xy}\tau_{xy}\mathrm{d}V \\ &= \frac{1}{2}\int_x \frac{V_y(x)^2}{GA}\left(\frac{A}{I^2}\int_A \frac{Q(y)^2}{t(y)^2}\mathrm{d}A\right)\mathrm{d}x \end{aligned} \tag{1}$$

where the variable $V_y(x)$ is the shear force, $Q(y)$ is the moment of the area about the z-axis, $t(y)$ is the beam thickness along the z-direction, I_y is the area moment of inertia of beam cross section (having area A) about the z-axis, and G is the shear modulus.

Considering

$$\frac{1}{\kappa_{xy}} = \left(\frac{A}{I_y^2}\int_A \frac{Q(y)^2}{t(y)^2}\mathrm{d}A\right) \tag{2}$$

where the symbol κ_{xy} is called the shear form factor in the x–y plane

$$U_s = \frac{1}{2}\int_x \frac{V_y(x)^2}{\kappa_{xy}GA}\mathrm{d}x = \frac{1}{2}\int_x \bar{\gamma}_{xy}\bar{\tau}_{xy}(\kappa_{xy}A)\mathrm{d}x \tag{3}$$

Therefore, the average strain and stress from an energy point of view are defined as follows

$$\left.\begin{aligned} \bar{\gamma}_{xy} &= \frac{V_y}{G(\kappa_{xy}A)}; \quad \bar{\tau}_{xy} = \frac{V_y}{\kappa_{xy}A} \\ \bar{\gamma}_{xz} &= \frac{V_z}{G(\kappa_{xz}A)}; \quad \bar{\tau}_{xz} = \frac{V_z}{\kappa_{xz}A} \end{aligned}\right\} \tag{4}$$

Now, the strain equivalent (Figure 1) terms for a beam consisting of bending curvature and the shear strains are

$$\{\varepsilon\} = \begin{bmatrix} \dfrac{\partial\theta_y}{\partial x} & \dfrac{\partial\theta_z}{\partial x} & \bar{\gamma}_{xy} & \bar{\gamma}_{xz} \end{bmatrix}^{\mathrm{T}} \tag{5}$$

The corresponding stress resultant terms are

$$\{\sigma\} = \begin{bmatrix} M_y & M_z & V_y & V_z \end{bmatrix}^{\mathrm{T}} \tag{6}$$

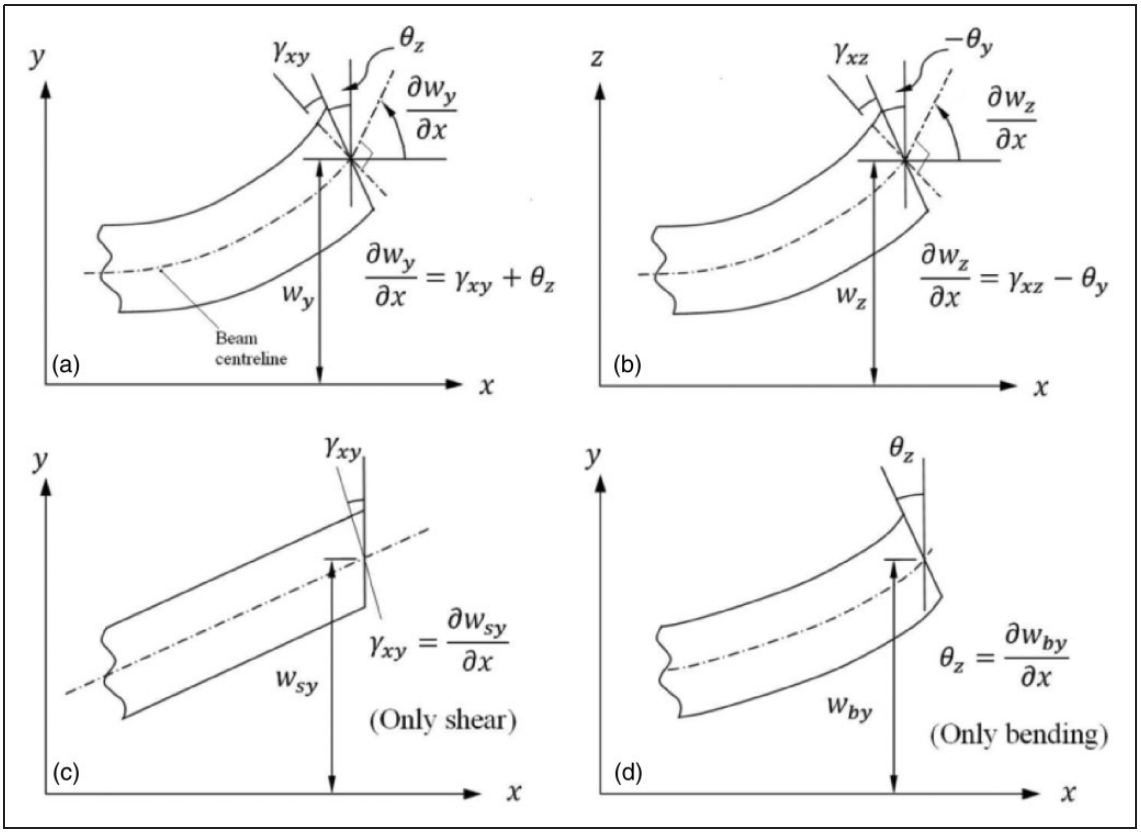

Figure 1. Total deformation in (a) plane x–y and (b) plane x–z; (c) shear and (d) bending deformations in plane x–y, where the total displacement (w_y) in the x–y plane consists of displacement due to shear (w_{sy}) and displacement due to bending (w_{by}).

where

$$\left.\begin{aligned} M_y &= \int_A \sigma z \mathrm{d}A = \int_A E z^2 \frac{\partial \theta_y}{\partial x} \mathrm{d}A \\ M_z &= \int_A -\sigma y \mathrm{d}A = \int_A E y^2 \frac{\partial \theta_z}{\partial x} \mathrm{d}A \end{aligned}\right\} \tag{6a}$$

For an elastic material, the relation between stress resultants and strain equivalent terms is given by

$$\begin{Bmatrix} M_y \\ M_z \\ V_y \\ V_z \end{Bmatrix} = \begin{bmatrix} EI_y & & & \\ & EI_z & & \\ & & \kappa_{xy}AG & \\ & & & \kappa_{xz}AG \end{bmatrix} \begin{Bmatrix} \partial\theta_y/\partial x \\ \partial\theta_z/\partial x \\ \bar{\gamma}_{xy} \\ \bar{\gamma}_{xz} \end{Bmatrix} \tag{7}$$

2.1.2. Stress–strain relations for viscoelastic Timoshenko beam. Figure 2 shows a Maxwell–Wiechert model with multiple parallel branches. For the purpose of analysis a Maxwell–Wiechert model with a single Maxwell branch is considered first. The principle is then extended for multiple branches. A Maxwell branch here represents the relation not only between normal stress and strain but also between two shear stresses and corresponding shear strains. The stress–strain relations are as follows

$$\left.\begin{aligned} \sigma &= E\varepsilon_c + \eta_{\varepsilon 1}(\dot{\varepsilon}_c - \dot{\varepsilon}_{b1}) \\ \tau_{xy} &= G\gamma_{xyc} + \eta_{\gamma xy1}\left(\dot{\gamma}_{xyc} - \dot{\gamma}_{xyb1}\right) \\ \tau_{xz} &= G\gamma_{xzc} + \eta_{\gamma xz1}(\dot{\gamma}_{xzc} - \dot{\gamma}_{xzb1}) \end{aligned}\right\} \tag{8}$$

with the constraint relations

$$\left.\begin{aligned} \eta_{\varepsilon 1}(\dot{\varepsilon}_c - \dot{\varepsilon}_{b1}) &= E_1\varepsilon_{b1} \\ \eta_{\gamma xy1}\left(\dot{\gamma}_{xyc} - \dot{\gamma}_{xyb1}\right) &= G_1\gamma_{xyb1} \\ \eta_{\gamma xz1}(\dot{\gamma}_{xzc} - \dot{\gamma}_{xzb1}) &= G_1\gamma_{xzb1} \end{aligned}\right\} \tag{9}$$

The subscripts "c" and "b" are used for actual strains and additional strains corresponding to internal damping variables, respectively.

Using Laplace transform and eliminating the internal damping variable, one can show that

$$\left.\begin{aligned} \tilde{\sigma}(s) &= \left\{E + \frac{\eta_{\varepsilon 1}s}{1 + s\eta_{\varepsilon 1}/E_1}\right\}\tilde{\varepsilon}_c(s) \\ \tilde{\tau}_{xy}(s) &= \left\{G + \frac{\eta_{\gamma xy1}s}{1 + s\eta_{\gamma xy1}/G_1}\right\}\tilde{\gamma}_c(s) \\ \tilde{\tau}_{xz}(s) &= \left\{G + \frac{\eta_{\gamma xz1}s}{1 + s\eta_{\gamma xz1}/G_1}\right\}\tilde{\gamma}_c(s) \end{aligned}\right\} \tag{10}$$

The constitutive relations are then imposed in the Laplace domain. Assuming incompressibility (Williams, 1964)

$$\left.\begin{aligned} \frac{\left\{E + \frac{\eta_{\varepsilon 1}s}{1+s\eta_{\varepsilon 1}/E_1}\right\}}{\left\{G + \frac{\eta_{\gamma xy1}s}{1+s\eta_{\gamma xy1}/G_1}\right\}} &= 2(1+\mu) = 3 \\ \frac{\left\{E + \frac{\eta_{\varepsilon 1}s}{1+s\eta_{\varepsilon 1}/E_1}\right\}}{\left\{G + \frac{\eta_{\gamma xz1}s}{1+s\eta_{\gamma xz1}/G_1}\right\}} &= 2(1+\mu) = 3 \end{aligned}\right\} \tag{11}$$

Equating the constants and coefficients of s

$$\left.\begin{aligned} E = 3G; \quad \eta_{\varepsilon 1} = 3\eta_{\gamma xy1}; \quad \frac{\eta_{\varepsilon 1}}{E_1} = \frac{\eta_{\gamma xy1}}{G_1}; \\ \eta_{\varepsilon 1} = 3\eta_{\gamma xz1}; \quad \frac{\eta_{\varepsilon 1}}{E_1} = \frac{\eta_{\gamma xz1}}{G_1} \end{aligned}\right\} \tag{12}$$

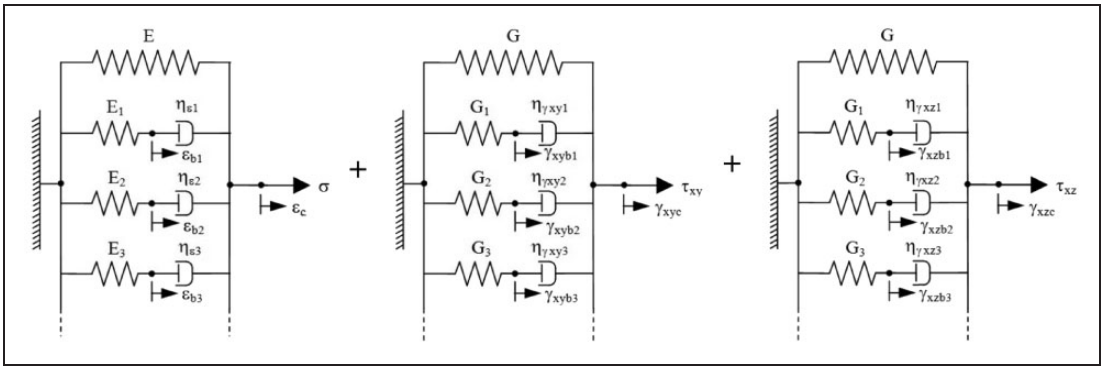

Figure 2. The Maxwell–Wiechert model with parallel branches considering shear deformation in x–y plane and x–z plane (E_i, G_i are the stiffness parameters and $\eta_{\varepsilon i}$, $\eta_{\gamma xyi}$, $\eta_{\gamma xzi}$ are the damping parameters of the ith branch corresponding to normal strain and shear strain (in x–y and x–z planes), respectively).

In terms of stress and strain equivalent terms, the material relations (equation (8)) are expressed as

$$\begin{Bmatrix} M_y \\ M_z \\ V_y \\ V_z \end{Bmatrix} = [D_e] \begin{Bmatrix} \partial\theta_{yc}/\partial x \\ \partial\theta_{zc}/\partial x \\ \bar{\gamma}_{xyc} \\ \bar{\gamma}_{xzc} \end{Bmatrix} + [D_{b1}] \left(\begin{Bmatrix} \partial\dot{\theta}_{yc}/\partial x \\ \partial\dot{\theta}_{zc}/\partial x \\ \dot{\bar{\gamma}}_{xyc} \\ \dot{\bar{\gamma}}_{xzc} \end{Bmatrix} - \begin{Bmatrix} \partial\dot{\theta}_{yb1}/\partial x \\ \partial\dot{\theta}_{zb1}/\partial x \\ \dot{\bar{\gamma}}_{xyb1} \\ \dot{\bar{\gamma}}_{xzb1} \end{Bmatrix} \right)$$

or

$$\{\sigma\} = [D_e]\{\varepsilon_c\} + [D_{b1}](\{\dot{\varepsilon}_c\} - \{\dot{\varepsilon}_{b1}\}) \tag{13}$$

where

$$[D_e] = \begin{bmatrix} EI_y & & & \\ & EI_z & & \\ & & \kappa_{xy}AG & \\ & & & \kappa_{xz}AG \end{bmatrix}$$

$$[D_{b1}] = \begin{bmatrix} \eta_{\varepsilon 1} I_y & & & \\ & \eta_{\varepsilon 1} I_z & & \\ & & \kappa_{xy} A \eta_{\gamma xy1} & \\ & & & \kappa_{xz} A \eta_{\gamma xz1} \end{bmatrix}$$

$$\{\varepsilon_c\} = \begin{bmatrix} \dfrac{\partial\theta_{yc}}{\partial x} & \dfrac{\partial\theta_{zc}}{\partial x} & \bar{\gamma}_{xyc} & \bar{\gamma}_{xzc} \end{bmatrix}^{\mathrm{T}}$$

$$\{\varepsilon_{b1}\} = \begin{bmatrix} \partial\theta_{yb1}/\partial x & \partial\theta_{zb1}/\partial x & \bar{\gamma}_{xyb1} & \bar{\gamma}_{xzb1} \end{bmatrix}^{\mathrm{T}}$$

The constraint relations (equation (9)) now become

$$[D_{b1}](\{\dot{\varepsilon}_c\} - \{\dot{\varepsilon}_{b1}\}) = [D_{e1}]\{\varepsilon_{b1}\} \tag{14}$$

where

$$[D_{e1}] = \begin{bmatrix} E_1 I_y & & & \\ & E_1 I_z & & \\ & & \kappa_{xy} A G_1 & \\ & & & \kappa_{xz} A G_1 \end{bmatrix}$$

2.1.3. Shape functions and strain–displacement relations. The actual strain equivalent terms (Figure 3) are derived from the displacement variables w_{yc} and w_{zc}

$$\begin{Bmatrix} w_{yc} \\ w_{zc} \\ \theta_{yc} \\ \theta_{zc} \end{Bmatrix} = [N] \begin{bmatrix} w_{yc1} & w_{zc1} & \theta_{yc1} & \theta_{zc1} & w_{yc2} & w_{zc2} & \theta_{yc2} & \theta_{zc2} \end{bmatrix}^{\mathrm{T}} \tag{15}$$

where the shape function matrix is

$$[N] = \begin{bmatrix} N_{w_y 1} & 0 & 0 & N_{w_y 2} & N_{w_y 3} & 0 & 0 & N_{w_y 4} \\ 0 & N_{w_z 1} & N_{w_z 2} & 0 & 0 & N_{w_z 3} & N_{w_z 4} & 0 \\ 0 & N_{\theta_y 1} & N_{\theta_y 2} & 0 & 0 & N_{\theta_y 3} & N_{\theta_y 4} & 0 \\ N_{\theta_z 1} & 0 & 0 & N_{\theta_z 2} & N_{\theta_z 3} & 0 & 0 & N_{\theta_z 4} \end{bmatrix}$$

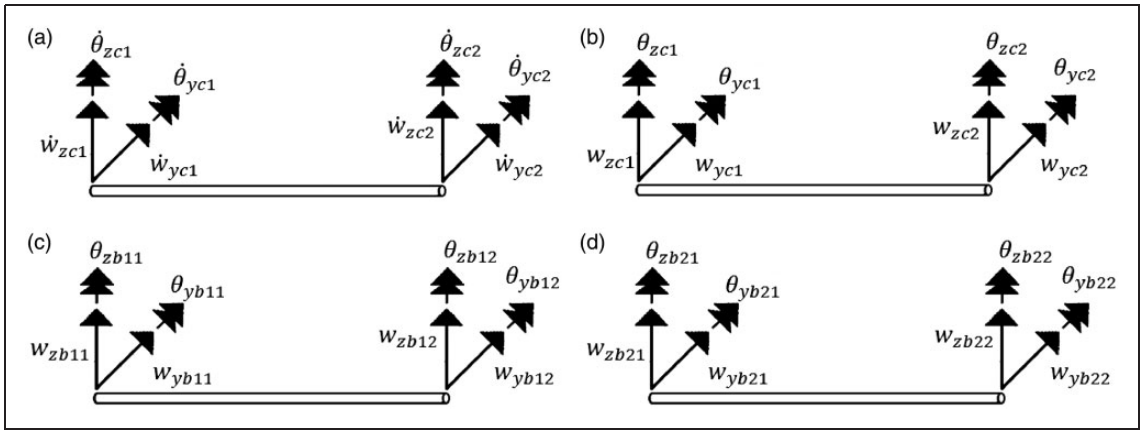

Figure 3. Degrees of freedom of the proposed element with two Maxwell branches is composed of (a) velocity degrees of freedom, (b) usual degrees of freedom, (c) damping degrees of freedom for the first Maxwell branch, (d) damping degrees of freedom for the second Maxwell branch.

Again

$$\{\varepsilon_c\} = \begin{Bmatrix} \partial\theta_{yc}/\partial x \\ \partial\theta_{zc}/\partial x \\ \bar{\gamma}_{xyc} \\ \bar{\gamma}_{xzc} \end{Bmatrix} = [B]\{U_c\} \tag{16}$$

where

$$[B] = \begin{bmatrix} 0 & \frac{\partial N_{\theta_y 1}}{\partial x} & \frac{\partial N_{\theta_y 2}}{\partial x} & 0 & 0 & \frac{\partial N_{\theta_y 3}}{\partial x} & \frac{\partial N_{\theta_y 4}}{\partial x} & 0 \\ \frac{\partial N_{\theta_z 1}}{\partial x} & 0 & 0 & \frac{\partial N_{\theta_z 2}}{\partial x} & \frac{\partial N_{\theta_z 3}}{\partial x} & 0 & 0 & N_{\theta_z 4} \\ \frac{\partial N_{w_y 1}}{\partial x} - N_{\theta_z 1} & 0 & 0 & \frac{\partial N_{w_y 2}}{\partial x} - N_{\theta_z 2} & \frac{\partial N_{w_y 3}}{\partial x} - N_{\theta_z 3} & 0 & 0 & \frac{\partial N_{w_y 4}}{\partial x} - N_{\theta_z 4} \\ 0 & \frac{\partial N_{w_z 1}}{\partial x} + N_{\theta_y 1} & \frac{\partial N_{w_z 2}}{\partial x} + N_{\theta_y 2} & 0 & 0 & \frac{\partial N_{w_z 3}}{\partial x} + N_{\theta_y 3} & \frac{\partial N_{w_z 4}}{\partial x} + N_{\theta_y 4} & 0 \end{bmatrix}$$

$$\{U_c\} = \begin{bmatrix} w_{yc1} & w_{zc1} & \theta_{yc1} & \theta_{zc1} & w_{yc2} & w_{zc2} & \theta_{yc2} & \theta_{zc2} \end{bmatrix}^{\mathrm{T}}$$

The shape functions are derived using the procedure shown by Bazoune and Khulief (2003). Some minor deviations in the signs of the shape functions are noted due to different sign conventions used in the present work and the above paper. The shape functions on the x–y plane are

$$\left.\begin{aligned} N_{w_y 1} &= \bar{\Phi}_z(1 - 3\xi^2 + 2\xi^3 + \Phi_z(1-\xi)) \\ N_{w_y 2} &= l\bar{\Phi}_z(\xi - 2\xi^2 + \xi^3 + \frac{\Phi_z}{2}(\xi - \xi^2)) \\ N_{w_y 3} &= \bar{\Phi}_z(3\xi^2 - 2\xi^3 + \Phi_z\xi) \\ N_{w_y 4} &= l\bar{\Phi}_z(-\xi^2 + \xi^3 + \tfrac{\Phi_z}{2}(-\xi + \xi^2)) \end{aligned}\right\} \tag{17a}$$

$$\left.\begin{aligned} N_{\theta_z 1} &= \frac{6\bar{\Phi}_z}{l}(-\xi + \xi^2) \\ N_{\theta_z 2} &= \bar{\Phi}_z(1 - 4\xi + 3\xi^2 + \Phi_z(1-\xi)) \\ N_{\theta_z 3} &= -\tfrac{6\bar{\Phi}_z}{l}(-\xi + \xi^2) \\ N_{\theta_z 4} &= \bar{\Phi}_z(-2\xi + 3\xi^2 + \Phi_z\xi) \end{aligned}\right\} \tag{17b}$$

where $\xi = x/l$, $\Phi_z = \frac{12EI_z}{\kappa GAl^2}$, and $\bar{\Phi}_z = \frac{1}{1+\Phi_z}$.

Similarly the shape functions on the x–z plane are

$$\left.\begin{aligned} N_{w_z 1} &= \bar{\Phi}_y(1 - 3\xi^2 + 2\xi^3 + \Phi_y(1-\xi)) \\ N_{w_z 2} &= -l\bar{\Phi}_y(\xi - 2\xi^2 + \xi^3 + \frac{\Phi_y}{2}(\xi - \xi^2)) \\ N_{w_z 3} &= \bar{\Phi}_y(3\xi^2 - 2\xi^3 + \Phi_y\xi) \\ N_{w_z 4} &= -l\bar{\Phi}_y(-\xi^2 + \xi^3 + \tfrac{\Phi_y}{2}(-\xi + \xi^2)) \end{aligned}\right\} \tag{17c}$$

$$\left.\begin{aligned} N_{\theta_y 1} &= -\tfrac{6\bar{\Phi}_y}{l}(-\xi + \xi^2) \\ N_{\theta_y 2} &= \bar{\Phi}_y(1 - 4\xi + 3\xi^2 + \Phi_z(1-\xi)) \\ N_{\theta_y 3} &= \tfrac{6\bar{\Phi}_y}{l}(-\xi + \xi^2) \\ N_{\theta_y 4} &= \bar{\Phi}_y(-2\xi + 3\xi^2 + \Phi_y\xi) \end{aligned}\right\} \tag{17d}$$

where $\Phi_y = \frac{12EI_y}{\kappa GAl^2}$ and $\bar{\Phi}_y = \frac{1}{1+\Phi_y}$.

Now, it is assumed that the additional damping variables are also interpolated from additional nodal degrees of freedom using the same shape functions. Therefore

$$\begin{Bmatrix} w_{yb1} \\ w_{zb1} \\ \theta_{zb1} \\ \theta_{yb1} \end{Bmatrix} = [N]\{U_{b1}\} \tag{18}$$

where

$$\{U_{b1}\} = \begin{bmatrix} w_{yb11} & w_{zb11} & \theta_{yb11} & \theta_{zb11} & w_{yb12} & w_{zb12} & \theta_{yb12} & \theta_{zb12} \end{bmatrix}^{\mathrm{T}}$$

$$\{\varepsilon_{b1}\} = \begin{Bmatrix} \partial\theta_{yb1}/\partial x \\ \partial\theta_{zb1}/\partial x \\ \bar{\gamma}_{xyb1} \\ \bar{\gamma}_{xzb1} \end{Bmatrix} = [B]\{U_{b1}\} \tag{19}$$

The matrix $[B]$ is the standard strain–displacement matrix for a 3D Timoshenko beam element, as given in equation (16).

2.1.4. Derivation of finite element equations from the principle of virtual work. Now, the finite element equations are derived from the principle of virtual work. The virtual strain energy is equated to the virtual work done by inertia forces and external forces. Using equations (13) and (16), the virtual strain

energy is

$$\int_l \{\delta\varepsilon_c\}^{\mathrm{T}}\{\sigma\}\mathrm{d}x = \{\delta U_c\}^{\mathrm{T}}\int_l [B]^{\mathrm{T}}[D_e][B]\mathrm{d}x\{U_c\} + \{\delta U_c\}^{\mathrm{T}}\int_l [B]^{\mathrm{T}}[D_{b1}][B]\mathrm{d}x\{\dot{U}_c\} - \{\delta U_c\}^{\mathrm{T}}\int_l [B]^{\mathrm{T}}[D_{b1}][B]\mathrm{d}x\{\dot{U}_{b1}\} \quad (20)$$

or

$$\int_V \{\delta\varepsilon_c\}^{\mathrm{T}}\{\sigma\}\mathrm{d}V = \{\delta U_c\}^{\mathrm{T}}[K_e^e]\{U_c\} + \{\delta U_c\}^{\mathrm{T}}[K_{b1}^e]\{\dot{U}_c\} - \{\delta U_c\}^{\mathrm{T}}[K_{b1}^e]\{\dot{U}_{b1}\} \quad (21)$$

where

$$[K_e^e] = \int_l [B]^{\mathrm{T}}[D_e][B]\mathrm{d}x \quad (22a)$$

$$[K_{b1}^e] = \int_l [B]^{\mathrm{T}}[D_{b1}][B]\mathrm{d}x \quad (22b)$$

The virtual work done by the inertia force and gyroscopic moment in the spinning frame can be written as

$$-\{\delta U_c\}^{\mathrm{T}}\left(([M_T^e]+[M_R^e])\{\ddot{U}_c\} + 2\omega[\hat{M}_T^e]\{\dot{U}_c\} - \omega^2([M_T^e]-[M_R^e])\{U_c\}\right) \quad (23)$$

The inertia force expressions are taken from Nelson (1980). The variable ω stands for the spin speed of the rotor.

Virtual work done by external force $\{f^e\}$ is

$$\{\delta U_c\}^{\mathrm{T}}\{f^e\} \quad (24)$$

The virtual strain energy equals the virtual work done by inertia force, gyroscopic moment and external force. Combining equations (21), (23), and (24), the following equation is obtained

$$([M_T^e]+[M_R^e])\{\ddot{U}_c\} + 2\omega[\hat{M}_T^e]\{\dot{U}_c\} - \omega^2([M_T^e]-[M_R^e])\{U_c\} + [K_e^e]\{U_c\} + [K_{b1}^e]\{\dot{U}_c\} - [K_{b1}^e]\{\dot{U}_{b1}\} = \{0\} \quad (25)$$

Pre-multiplying the constraint relation (equation (14)) by $\{\delta\varepsilon_c\}^{\mathrm{T}}$ and integrating it over the length

$$\int_l \{\delta\varepsilon_c\}^{\mathrm{T}}[D_{b1}](\{\dot{\varepsilon}_c\}-\{\dot{\varepsilon}_{b1}\})\mathrm{d}x = \int_l \{\delta\varepsilon_c\}^{\mathrm{T}}[D_{e1}]\{\varepsilon_{b1}\}\mathrm{d}x \quad (26)$$

or

$$\int_l [B]^{\mathrm{T}}[D_{b1}][B]\{\dot{U}_c\}\mathrm{d}x - \int_l [B]^{\mathrm{T}}[D_{b1}][B]\{\dot{U}_{b1}\}\mathrm{d}x = \int_l [B]^{\mathrm{T}}[D_{e1}][B]\{U_{b1}\}\mathrm{d}x \quad (27)$$

or

$$[K_{e1}^e]\{U_{b1}\} - [K_{b1}^e]\{\dot{U}_c\} + [K_{b1}^e]\{\dot{U}_{b1}\} = 0 \quad (28)$$

where

$$[K_{e1}^e] = \int_l [B]^{\mathrm{T}}[D_{e1}][B]\mathrm{d}x \quad (29)$$

Now, combining equations (25) and (28) one obtains

$$\begin{bmatrix} [M_T^e]+[M_R^e] & [0] & -[K_{b1}^e] \\ [0] & [I] & [0] \\ [0] & [0] & [K_{b1}^e] \end{bmatrix} \begin{Bmatrix} \{\ddot{U}_c\} \\ \{\dot{U}_c\} \\ \{\dot{U}_{b1}\} \end{Bmatrix} + \begin{bmatrix} 2\omega[\hat{M}_T^e]+[K_{b1}^e] & -\omega^2([M_T^e]-[M_R^e])+[K_e^e] & [0] \\ -[I] & [0] & [0] \\ -[K_{b1}^e] & [0] & [K_{e1}^e] \end{bmatrix} \times \begin{Bmatrix} \{\dot{U}_c\} \\ \{U_c\} \\ \{U_{b1}\} \end{Bmatrix} = \begin{Bmatrix} \{f^e\} \\ 0 \\ 0 \end{Bmatrix} \quad (30)$$

The detailed expressions for the matrices are given in Appendix 1.

2.1.5. Generalization for more than one Maxwell branches. For two Maxwell branches one more damping variable w_{b2} is considered. Now, it is assumed that this damping variable is also interpolated from additional nodal degrees of freedom. The governing

equation becomes

$$\begin{bmatrix} [M_T^e]+[M_R^e] & [0] & -[K_{b1}^e] & -[K_{b2}^e] \\ [0] & [I] & [0] & [0] \\ [0] & [0] & [K_{b1}^e] & [0] \\ [0] & [0] & [0] & [K_{b2}^e] \end{bmatrix} \begin{Bmatrix} \{\ddot{U}_c\} \\ \{\dot{U}_c\} \\ \{\dot{U}_{b1}\} \\ \{\dot{U}_{b2}\} \end{Bmatrix} + \begin{bmatrix} 2\omega[\hat{M}_T^e]+[K_{b1}^e]+[K_{b2}^e] & -\omega^2([M_T^e]-[M_R^e])+[K_e^e] & [0] & [0] \\ -[I] & [0] & [0] & [0] \\ -[K_{b1}^e] & [0] & [K_{e1}^e] & [0] \\ -[K_{b2}^e] & [0] & [0] & [K_{e2}^e] \end{bmatrix} \times \begin{Bmatrix} \{\dot{U}_c\} \\ \{U_c\} \\ \{U_{b1}\} \\ \{U_{b2}\} \end{Bmatrix} = \begin{Bmatrix} \{f^e\} \\ 0 \\ 0 \\ 0 \end{Bmatrix} \tag{31}$$

where $[K_{b2}^e]$ and $[K_{e2}^e]$ are similar to $[K_{b1}^e]$ and $[K_{e1}^e]$ in form, respectively. Only the parameters of the first parallel branch are replaced by the parameters of the second parallel branch. For example, $\eta_{\varepsilon 1}$ in $[D_{b1}]$ is replaced by $\eta_{\varepsilon 2}$ in $[D_{b2}]$.

Similarly, for a model with three Maxwell branches one more damping variable w_{b3} is considered and it is assumed that this damping variable is also interpolated from additional nodal degrees of freedom. The governing equation becomes

$$\begin{bmatrix} [M_T^e]+[M_R^e] & [0] & -[K_{b1}^e] & -[K_{b2}^e] & -[K_{b3}^e] \\ [0] & [I] & [0] & [0] & [0] \\ [0] & [0] & [K_{b1}^e] & [0] & [0] \\ [0] & [0] & [0] & [K_{b2}^e] & [0] \\ [0] & [0] & [0] & [0] & [K_{b3}^e] \end{bmatrix} \begin{Bmatrix} \{\ddot{U}_c\} \\ \{\dot{U}_c\} \\ \{\dot{U}_{b1}\} \\ \{\dot{U}_{b2}\} \\ \{\dot{U}_{b3}\} \end{Bmatrix} + \begin{bmatrix} 2\omega[\hat{M}_T^e]+[K_{b1}^e]+[K_{b2}^e]+[K_{b3}^e] & -\omega^2([M_T^e]-[M_R^e])+[K_e^e] & [0] & [0] & [0] \\ -[I] & [0] & [0] & [0] & [0] \\ -[K_{b1}^e] & [0] & [K_{e1}^e] & [0] & [0] \\ -[K_{b2}^e] & [0] & [0] & [K_{e2}^e] & [0] \\ -[K_{b3}^e] & [0] & [0] & [0] & [K_{e3}^e] \end{bmatrix} \begin{Bmatrix} \{\dot{U}_c\} \\ \{U_c\} \\ \{U_{b1}\} \\ \{U_{b2}\} \\ \{U_{b3}\} \end{Bmatrix} = \begin{Bmatrix} \{f^e\} \\ \{0\} \\ \{0\} \\ \{0\} \\ \{0\} \end{Bmatrix} \tag{32}$$

2.1.6. Extracting the parameters of the parallel Maxwell elements. For the viscoelastic materials ABS and PPC, frequency sweep tests were done in the DMA machine to obtain the values of storage modulus and loss modulus at different frequencies. Then the parameters of the parallel branches of the Maxwell–Wiechert model were calculated by curve fitting. The parameters of the model were determined using a nonlinear least squares technique (Recktenwal, 2007; Walking Randomly, 2013). The values of the parameters of the parallel branches, namely the spring stiffness and damping coefficient, as obtained by the above optimization technique, are tabulated in Tables 1 and 2. The plots of the storage modulus (E_s) and loss modulus (E_l) against frequency showing both the experimental data and the curves obtained using the extracted parameters are shown in Figures 4 and 5. It is observed that the Maxwell–Wiechert model with three parallel branches closely matches the experimental data.

2.2. Rigid disk element

A rigid disk element is essentially a point mass having translational and rotational inertia along the two transverse axes and generates a gyroscopic effect (Nelson and McVaugh, 1976; Nelson, 1980). It is a single node element having diagonal inertia matrices and affecting only the translational and rotational accelerations. It does not contribute to the stiffness matrix.

2.2.1. A validation strategy in the frequency domain. The present formulation is intended for computation of the time response of viscoelastic rotors. However, a harmonic solution in frequency domain can be used for validation of the code. There are two routes for a frequency domain analysis. The first or the conventional

Table 1. Values of the extracted parameters in a three parallel element Maxwell–Wiechert model for ABS.

Material	E (N/m^2)	E_1 (N/m^2)	E_2 (N/m^2)	E_3 (N/m^2)	η_1 (Ns/m^2)	η_2 (N s/m^2)	η_3 (N s/m^2)
ABS	1.648×10^9	3.642×10^7	2.1436×10^7	9.9369×10^8	5.333×10^6	2.1067×10^5	5.8395×10^4

Table 2. Values of the extracted parameters in a three parallel element Maxwell–Wiechert model for PPC.

Material	E (N/m^2)	E_1 (N/m^2)	E_2 (N/m^2)	E_3 (N/m^2)	η_1 (N s/m^2)	η_2 (N s/m^2)	η_3 (N s/m^2)
PPC	1.28×10^9	1.104×10^8	5.469×10^7	1.986×10^8	1.087×10^7	3.879×10^5	1.205×10^5

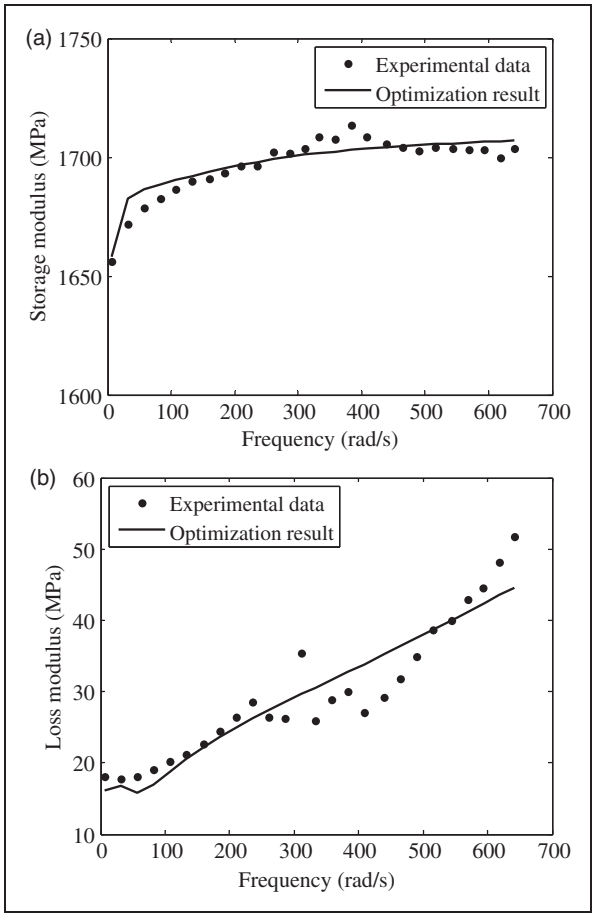

Figure 4. The experimental data and optimized curve obtained using the parameters listed in Table 1 of (a) storage modulus and (b) loss modulus of ABS.

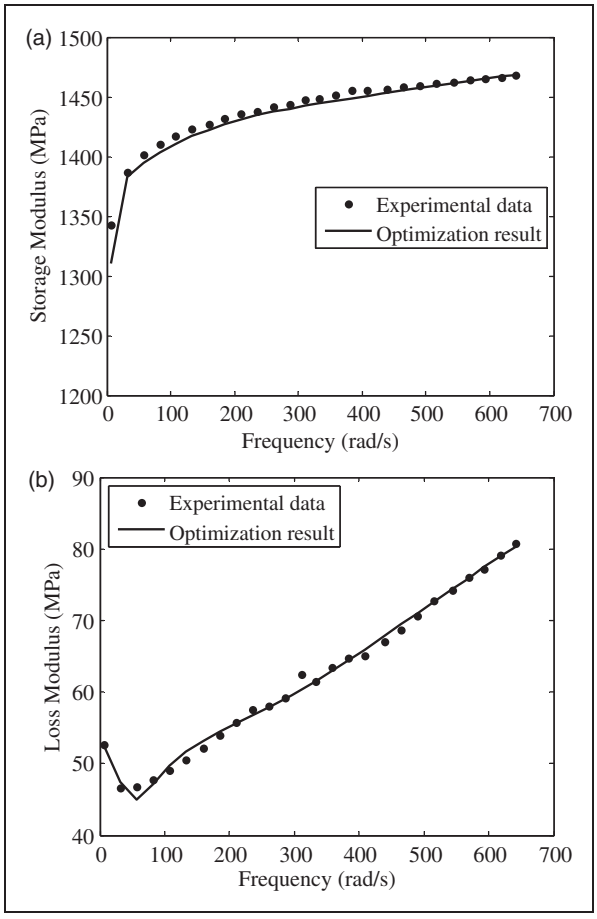

Figure 5. The experimental data and optimized curve obtained using the parameters listed in Table 2 of (a) storage modulus and (b) loss modulus of PPC.

one is to start with the following finite element equations without any damping degree of freedom

$$[M]\{\ddot{U}\} + [G]\{\dot{U}\} + +E[\bar{K}]\{U\} + [K_1]\{U\} = \{F\} \quad (33)$$

Assuming harmonic excitation in the form $\{F\} = \{F_0\}e^{j\omega t}$, the displacement and complex material modulus are written as follows

$$\{U\} = \{U_0\}e^{j\omega t} \quad (34)$$

$$E = E_s(\omega)(1 + j\eta(\omega)) \quad (35)$$

$$E = E_S(\omega) + jE_I(\omega) \quad (36)$$

where

$$E_I(\omega) = E_s(\omega)\eta(\omega) \tag{36a}$$

The material modulus is expressed as a frequency-dependent complex number in terms of storage modulus and loss coefficient. The displacement $\{U_0\}$ is a complex number and can be determined from the following equation

$$\{U_0\} = \left\{E_s(\omega)(1 + j\eta(\omega))\left[\bar{K}\right] - \omega^2[M] + j\omega[G]\right\}^{-1}\{F_0\} \tag{37}$$

The alternative starts with the proposed or the state space form with additional damping degrees of freedom. The element equations for one, two, and three parallel branches are shown in equations (30), (33), and (37), respectively. Each of these equations can be assembled and written as follows

$$[A]\left\{\dot{Z}\right\} + [B]\{Z\} = \{R\} \tag{38}$$

Considering $\{R\} = \{R_0\}e^{j\omega t}$ and $\{Z\} = \{Z_0\}e^{j\omega t}$, one obtains

$$\{Z_0\} = (j\omega[A] + [B])^{-1}\{R_0\} \tag{39}$$

In equations (38) and (39), the matrices $[A]$ and $[B]$ do not depend on frequency.

The validation problems are explained in the Section 3.1.

3. Numerical study

3.1. Validation of the state-space viscoelastic formulation

Two different rotor–disk models are tried here to validate the state space viscoelastic finite element formulation. The first model has a single rigid disk while the second model uses two rigid disks on the same simply supported shaft. Both of these have been modelled using ABS and PPC as the shaft material. It is easier to check the proposed formulation in the frequency domain as the results can be directly compared with those obtained using equation (37) where a complex frequency-dependent material modulus is considered. For this case, the spin speed is kept at zero. A harmonic force of amplitude 1 N and varying frequency is applied at the location of the single disk in the first model and the left disk in the second model. A Maxwell–Wiechert model with three Maxwell branches has been used.

In rotor–disk model 1, a plastic rotor of 600 mm length and 60 mm diameter is considered (Figure 6). The disk has 1 kg mass and 100 mm radius of gyration

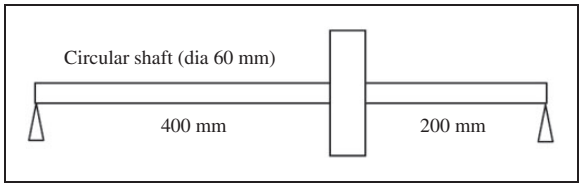

Figure 6. Rotor–disk model 1.

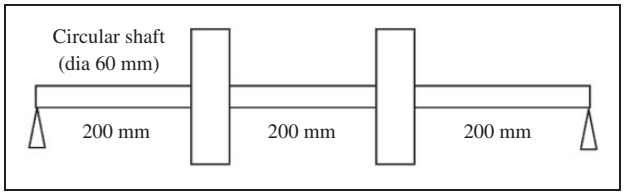

Figure 7. Rotor–disk model 2.

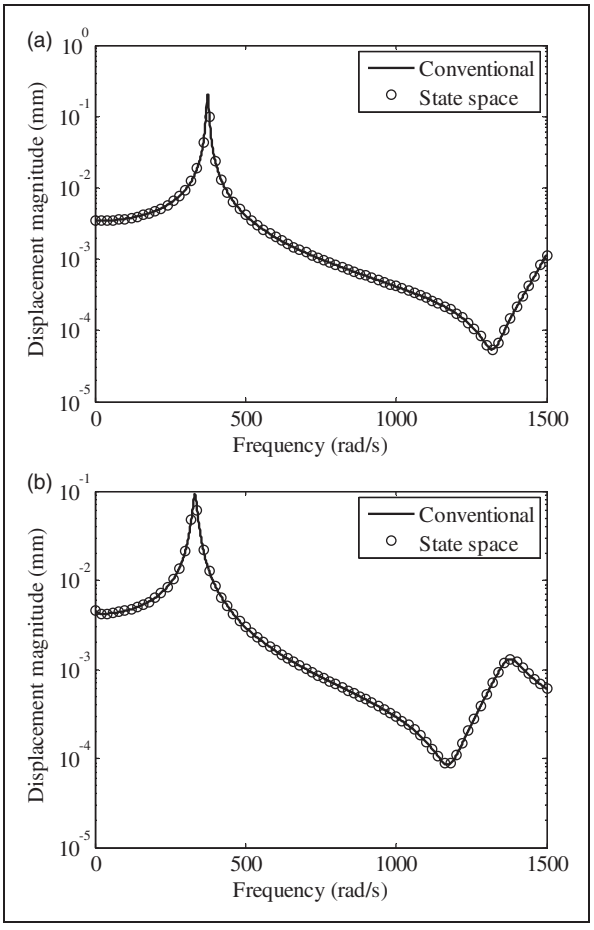

Figure 8. Frequency response computed using conventional frequency-dependent storage modulus and loss coefficient and state space viscoelastic model with additional damping degrees of freedom for rotor–disk model 1 with (a) ABC and (b) PPC as rotor material.

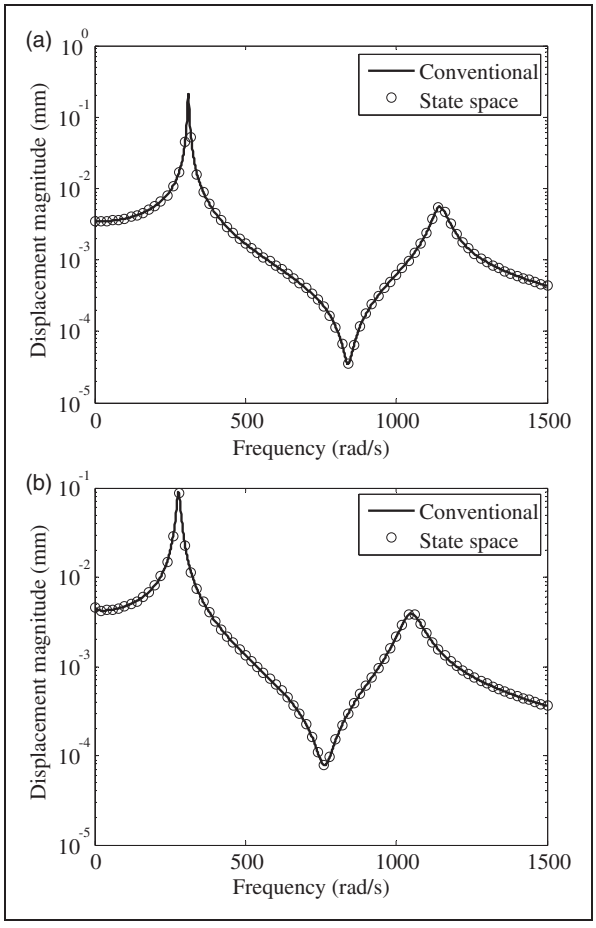

Figure 9. Frequency response computed using conventional frequency-dependent storage modulus and loss coefficient and state space viscoelastic model with additional damping degrees of freedom for rotor–disk model 2 with (a) ABS and (b) PPC as rotor material.

for polar moment of inertia. The rotor shaft is simply supported with the noncentral disk located at a distance of 400 mm from the left end support.

In rotor–disk model 2, a plastic rotor of 600 mm length and 60 mm diameter and fitted with two disks is considered (Figure 7). Both disks have a mass of 1 kg and 100 mm radius of gyration corresponding to polar moment of inertia. The rotor shaft is simply supported with the disks located at the trisection points at a distance of 200 mm and 400 mm from the left end support, respectively.

The frequency response plots obtained by using equation (37) and equation (39) are compared in Figures 8 and 9. They demonstrate exact agreement between the displacement spectrums with identical location and amplitude of the peaks.

3.2. Stability analysis

The proposed time-domain state space model can be used for stability analysis. For stability analysis, the eigenvalues of the homogeneous part of equation (32) (after assembly over elements) is computed. The largest real part of the eigenvalues and the Campbell diagram for the first mode are plotted in Figures 10 and 11 for shaft–disk model 1. In the presence of rotating viscoelastic damping, the largest real part becomes positive beyond a certain spin speed equal to the forward synchronous whirl frequency and renders the rotor–disk system unstable. Both ABS and PPC are considered as shaft materials.

3.3. Time response analysis

The time response of the rotor–disk systems at a particular spin speed is computed using equation (32). Two

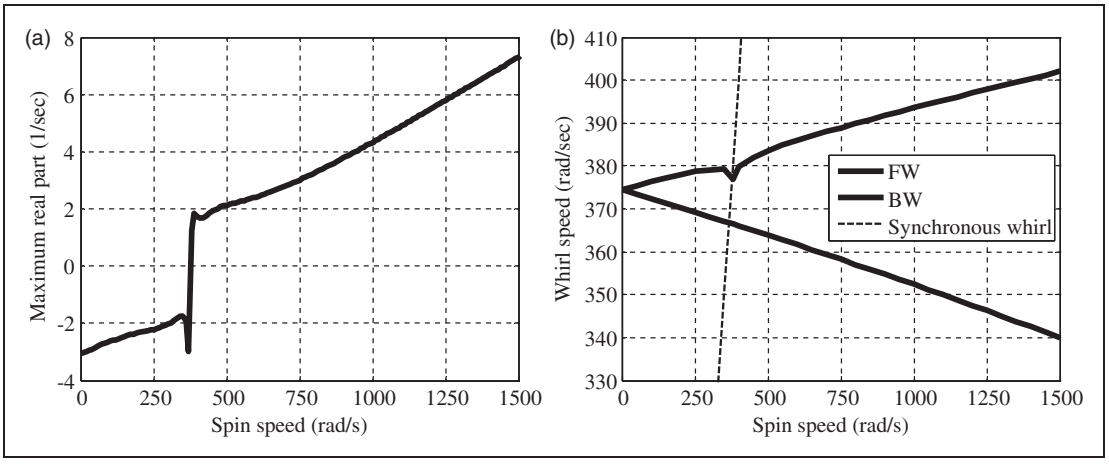

Figure 10. Rotor–disk model 1 with ABS as rotor material: (a) the largest real part of the eigenvalues are plotted against spin speed and (b) Campbell diagram for the first mode.

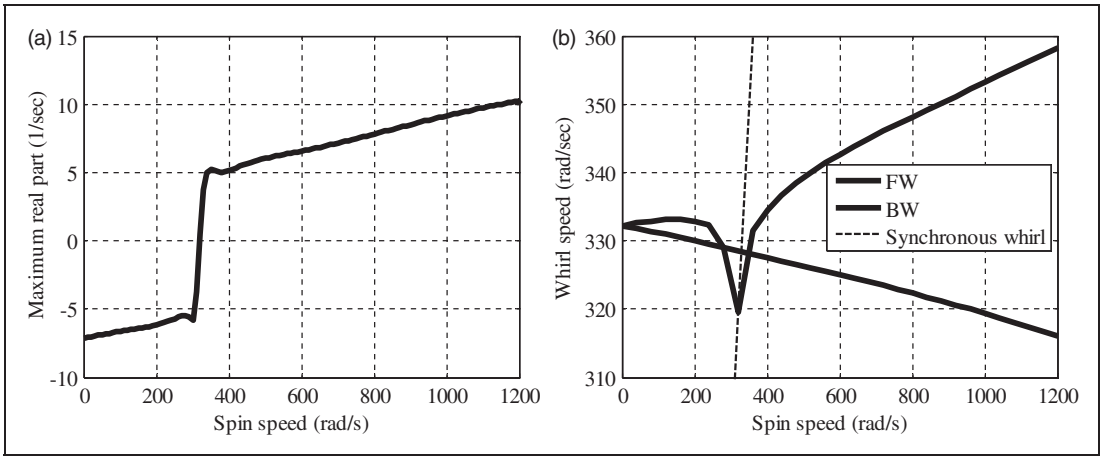

Figure 11. Rotor–disk model 1 with PPC as rotor material: (a) the largest real part of the eigenvalues are plotted against spin speed and (b) Campbell diagram for the first mode.

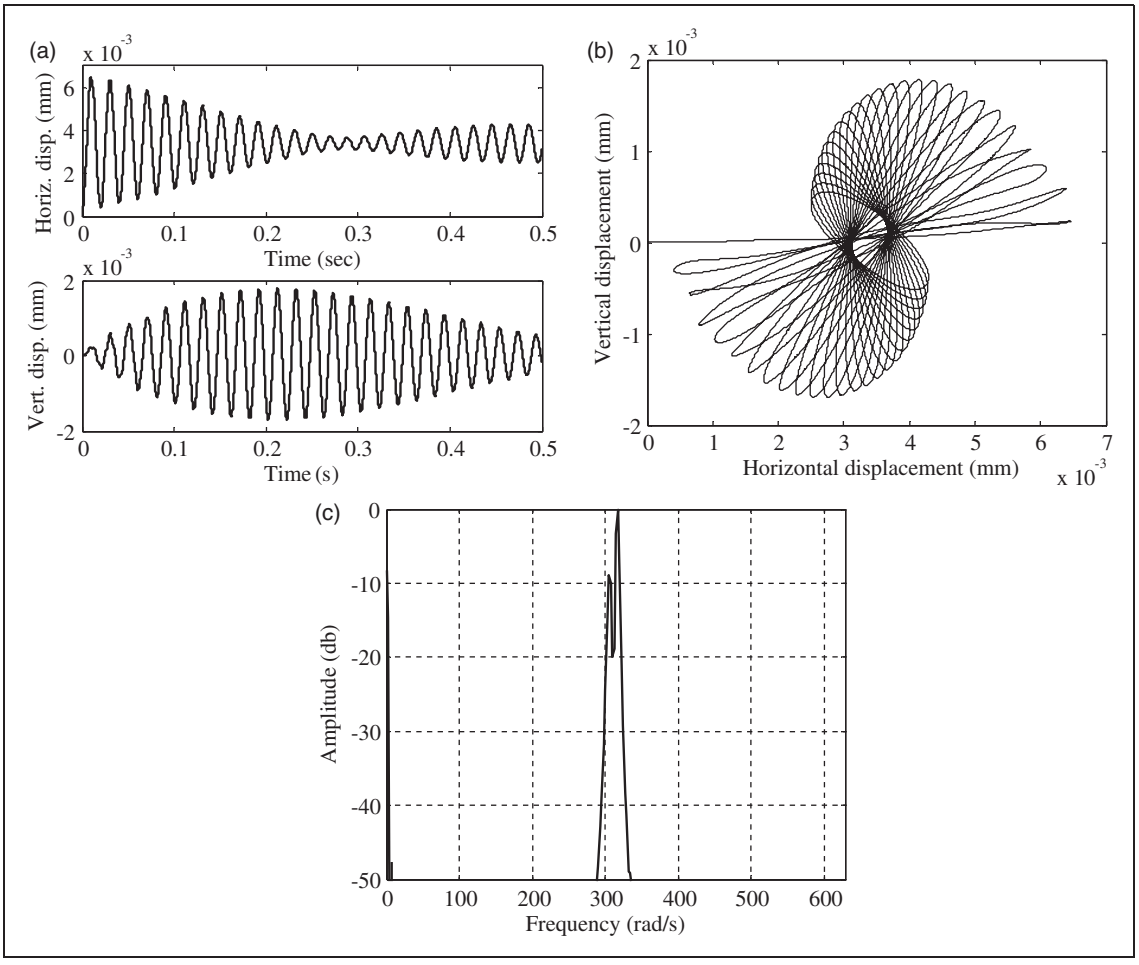

Figure 12. Time response to a horizontal unit step input (1 N) applied at the location of the left disk, showing (a) displacement, (b) whirl orbit and (c) FFT of rotor–disk model 2 with ABS as rotor material at a spin speed of 200 rad/s (subcritical zone).

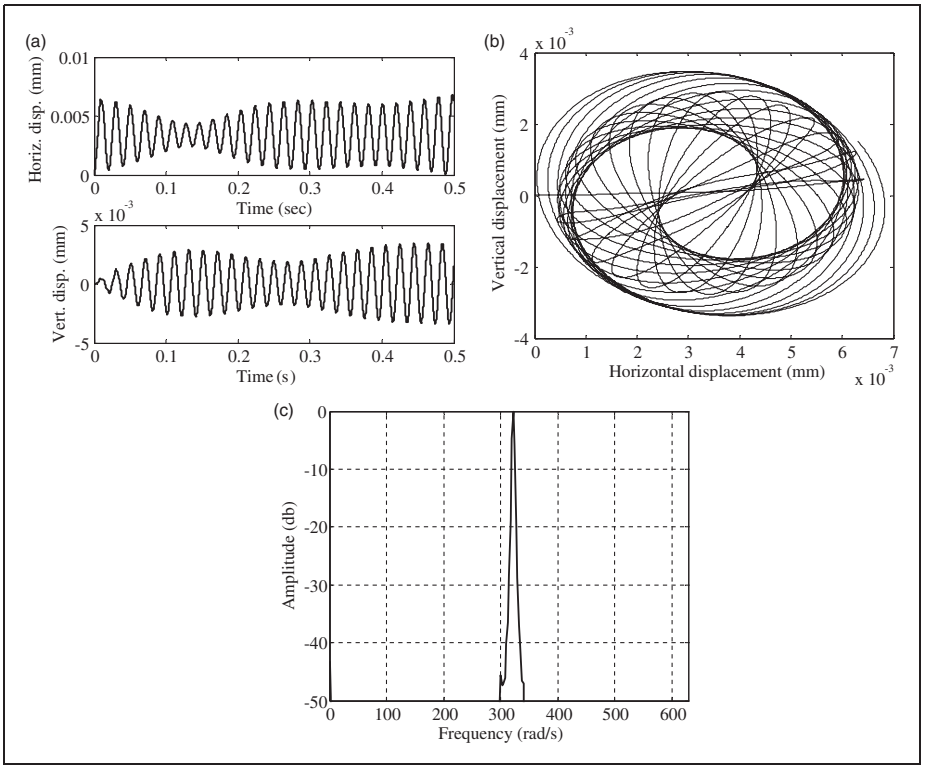

Figure 13. Time response to a horizontal unit step input (1 N) applied at the location of the left disk, showing (a) displacement, (b) whirl orbit and (c) FFT of rotor–disk model 2 with ABS as rotor material at a spin speed of 400 rad/s (supercritical zone).

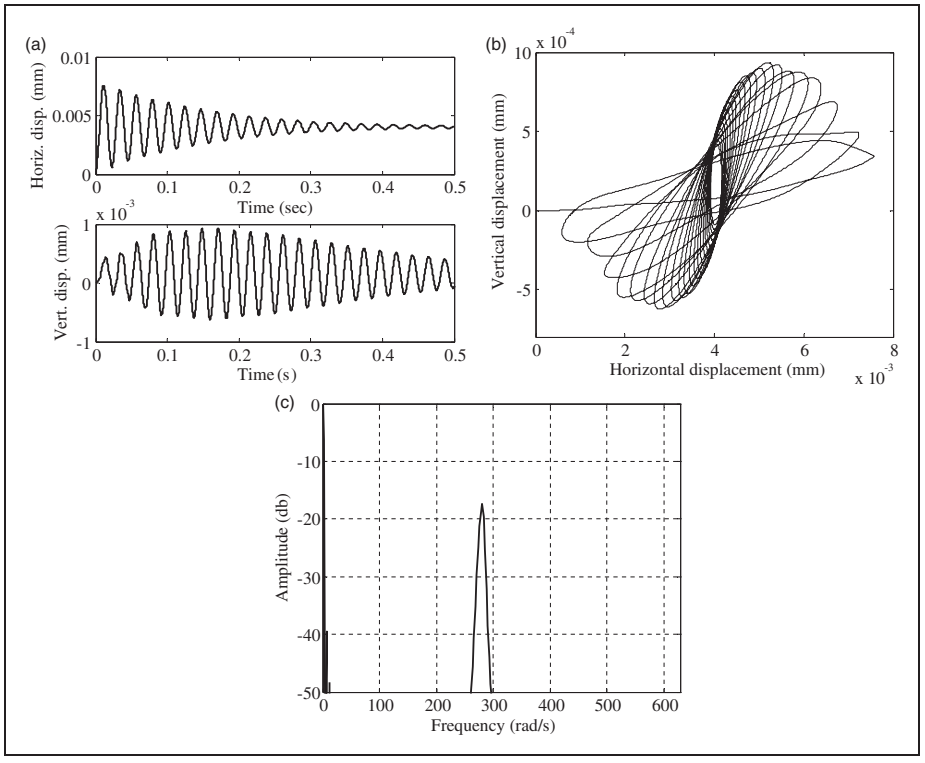

Figure 14. Time response to a horizontal unit step input (1 N) applied at the location of the left disk, showing (a) displacement, (b) whirl orbit and (c) FFT of rotor–disk model 2 with PPC as rotor material at a spin speed of 200 rad/s (subcritical zone).

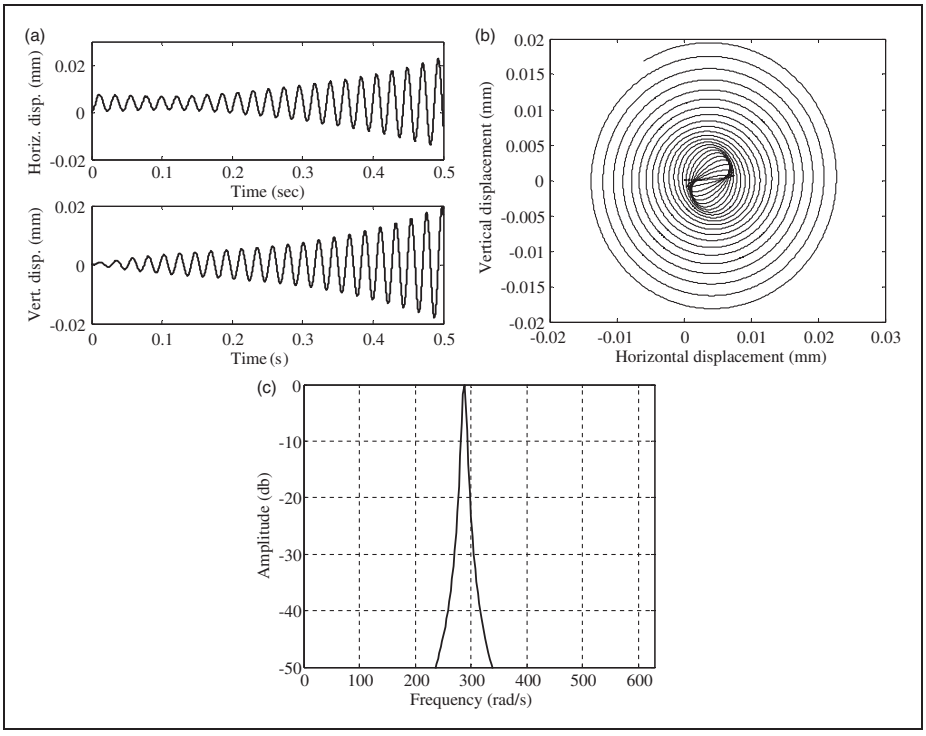

Figure 15. Time response to a horizontal unit step input (1 N) applied at the location of the left disk, showing (a) displacement, (b) whirl orbit and (c) FFT of rotor–disk model 2 with PPC as rotor material at a spin speed of 400 rad/s (supercritical zone).

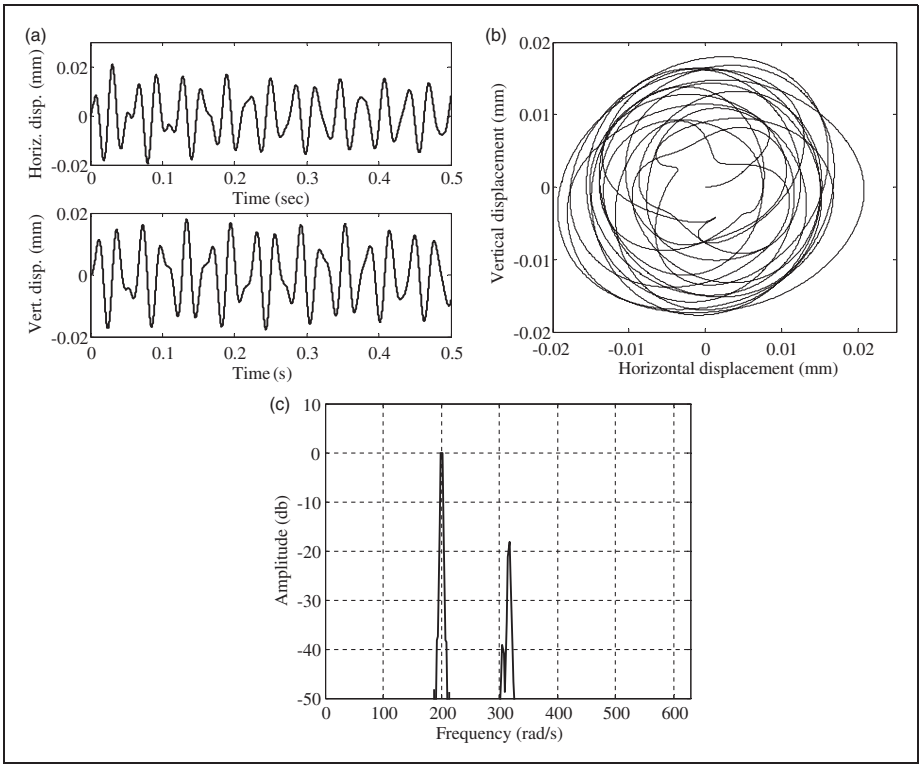

Figure 16. Time response to an imbalance applied at the location of the left disk, showing (a) displacement, (b) whirl orbit and (c) FFT of rotor–disk model 2 with ABS as rotor material at a spin speed of 200 rad/s (subcritical zone).

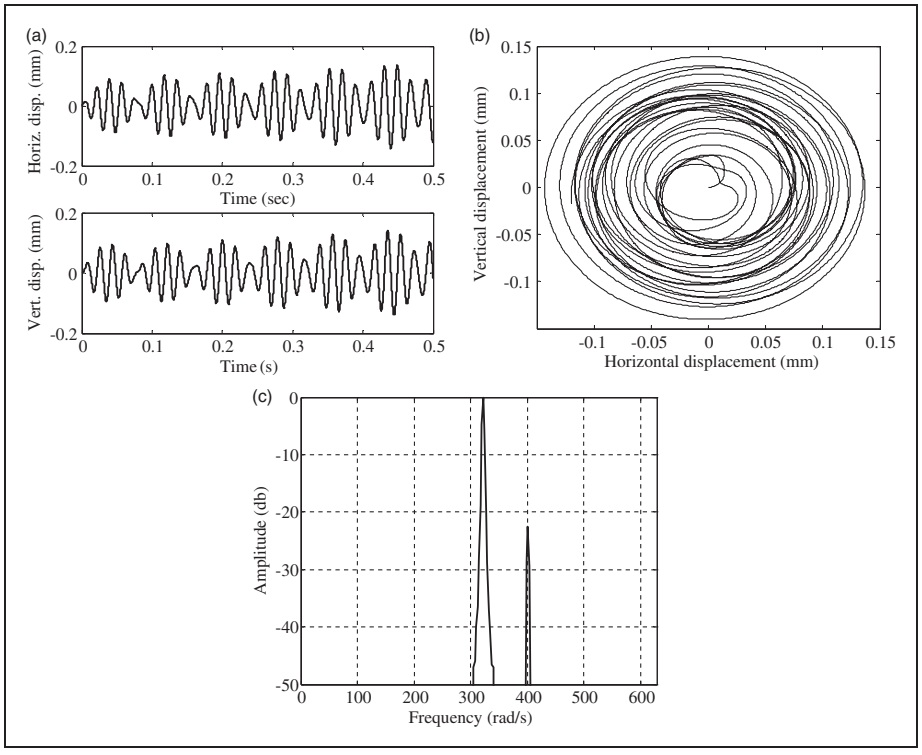

Figure 17. Time response to an imbalance applied at the location of the left disk, showing (a) displacement, (b) whirl orbit and (c) FFT of rotor–disk model 2 with ABS as rotor material at a spin speed of 400 rad/s (supercritical zone).

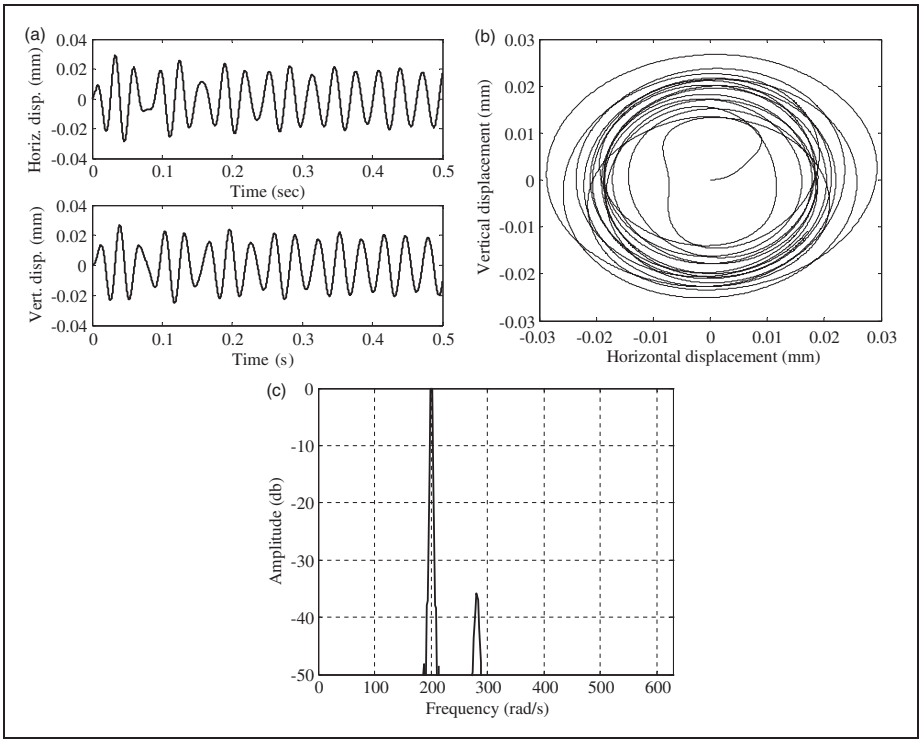

Figure 18. Time response to an imbalance applied at the location of the left disk, showing (a) displacement, (b) whirl orbit and (c) FFT of rotor–disk model 2 with PPC as rotor material at a spin speed of 200 rad/s (subcritical zone).

different force excitations are given: a horizontal unit step input (1 N) and an imbalance [unbalanced *mass*(m) $\times$ eccentricity(e) $= 5$ gm-cm]. Two spin speeds are considered in each case, one in the subcritical stable zone and another in the supercritical unstable zone. The horizontal and vertical displacements and the rotor orbit at the location of the disk are plotted in inertial frame. In addition, the fast Fourier transform (FFT) of the time response is presented. The same rotor–disk models with ABS and PPC as rotor materials are tried to illustrate the results.

The response of rotor–disk model 2, using ABS and PPC as rotor materials in both subcritical and supercritical conditions, to the horizontal unit step input (1 N) is depicted in Figures 12, 13, 14, and 15, respectively. The subcritical response is stable with the transient vibration dying out with time but the supercritical response is unstable as expected with the vibration amplitude increasing with time resulting in an ever increasing whirl orbit. The FFT shows the presence of both the forward and backward whirl modes with the former dominating the later in subcritical response of ABS. Since, the backward and forward whirl frequencies are close, beating is seen in the time response (Figure 12(a)). However, in case of PPC, only the forward mode is visible. This can be attributed to the higher material damping of PPC, as is evident from Figures 4(b) and 5(b). The backward mode has already died down for PPC in the time range considered for analysis. If the time span is increased the forward mode also decreases. For both the materials, the displacement finally reaches its steady state value. The supercritical response, for both the materials, shows only the forward whirl mode at which the system becomes unstable.

The response of rotor–disk model 2, using ABS and PPC as rotor material in both subcritical and supercritical conditions, to the imbalance ($m \times e = 5$ gm-cm) is depicted in Figures 16, 17, 18, and 19, respectively. The imbalance force acts like harmonic excitations in two mutually perpendicular transverse planes. The subcritical response is stable while the supercritical

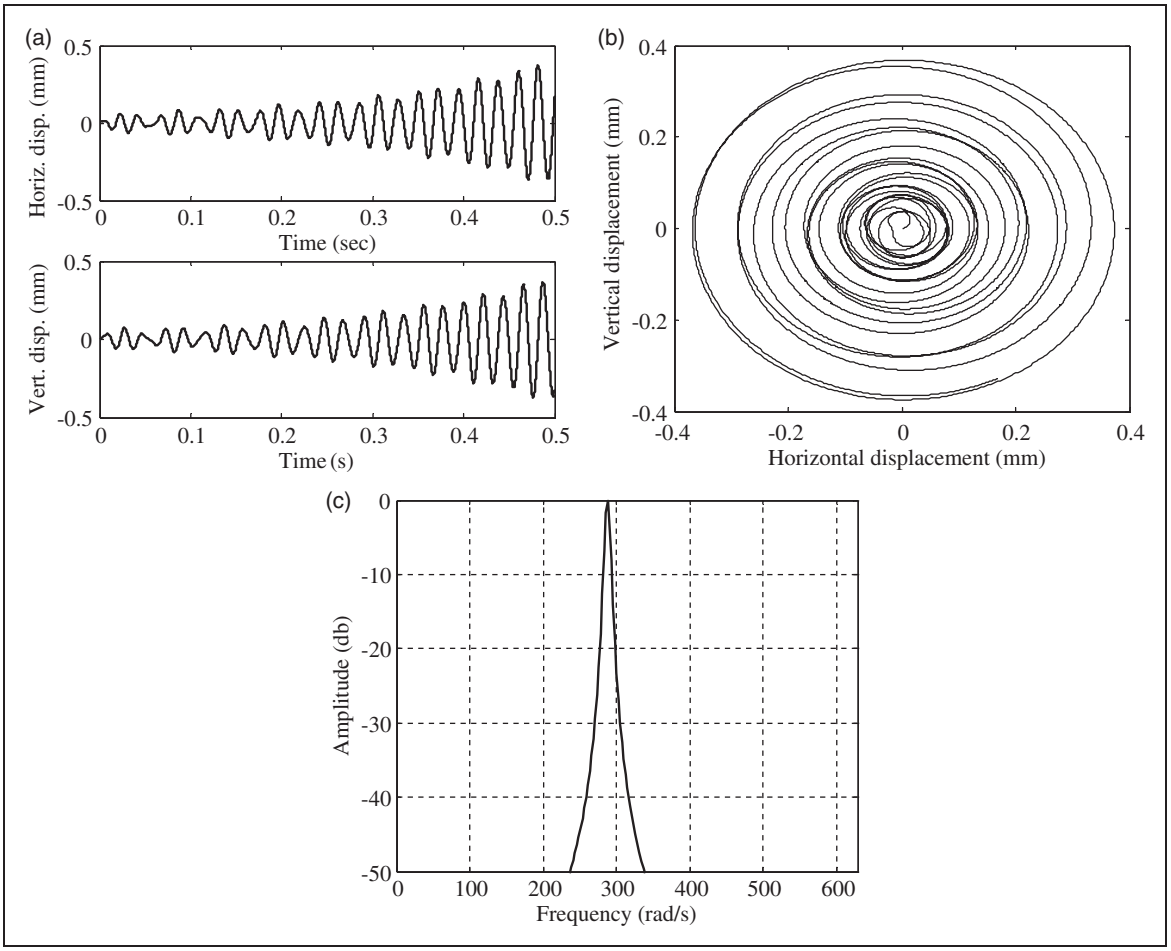

Figure 19. Time response to an unbalance applied at the location of the left disk, showing (a) displacement, (b) whirl orbit and (c) FFT of rotor–disk model 2 with PPC as rotor material at a spin speed of 400 rad/s (supercritical zone).

response is unstable as expected. The FFT shows the presence of synchronous whirl frequency as well as the forward natural frequency at that synchronous spin speed. In subcritical response the forcing frequency dominates over the forward whirl mode for both ABS and PPC. The forward mode slowly gets damped out. But in supercritical response the forward whirl mode becomes much more prominent. It is known that for material damping the forward mode becomes unstable and grows with time. The unstable response becomes much larger in comparison with the unbalance response.

4. Conclusion

- A Timoshenko shaft element has been developed for finite element analysis of viscoelastic rotors.
- In the finite element formulation, additional variables are interpolated so that the form of the augmented matrices remains systematic and simple.
- The parameters of the linear viscoelastic Maxwell–Wiechert model are extracted from laboratory tests using a nonlinear optimization technique.
- The proposed finite element technique is employed in stability analysis, construction of Campbell diagram, and response analysis in the time domain.

Declaration of Conflicting Interests

The author(s) declared no potential conflicts of interest with respect to the research, authorship, and/or publication of this article.

Funding

The author(s) received no financial support for the research, authorship, and/or publication of this article.

References

Adhikari S (2001) Eigenrelations for non-viscously damped systems. *AIAA Journal* 39: 1624–1630.

Adhikari S (2002) Dynamics of non-viscously damped linear systems. *Journal of Engineering Mechanics* 128: 328–339.

Adhikari S (2005) Qualitative dynamic characteristics of a non-viscously damped oscillator. *Proceedings of the Royal Society of London, Series A* 461: 2269–2288.

Adhikari S (2008) Dynamic response characteristics of a non-viscously damped oscillator. *Journal of Applied Mechanics* 75: 011003.

Adhikari S and Wagner N (2003) Analysis of a symmetric non-viscously damped linear dynamic system. *Journal of Applied Mechanics* 70: 885–893.

Bavastri CA, Ferreira EMS, De Espíndola JJ, et al. (2008) Modeling of dynamic rotors with flexible bearings due to the use of viscoelastic materials. *Journal of the Brazilian Society for Mechanical Sciience & Engineering* 30(1): 22–29.

Bazoune A and Khulief YA (2003) Shape functions of three-dimensional Timoshenko beam element. *Journal of Sound and Vibration* 259(2): 473–480.

Cavalini AA Jr, Galavotti TV, Morais TS, et al. (2011) Vibration attenuation in rotating machines using smart spring mechanism. *Mathematical Problems in Engineering* 2011: 1–14.

Cavalini AA Jr, Lobato FS, Koroishi EH, et al. (2015) Model updating of a rotating machine using the self-adaptive differential evolution algorithm. *Inverse Problems in Science and Engineering* 24(3): 504–523.

Dakel MZ, Baguet S and Dufour R (2014) Nonlinear dynamics of a support-excited flexible rotor with hydrodynamic journal bearings. *Journal of Sound and Vibration* 333(10): 2774–2799.

De Lima AMG, Stoppa MH, Rade DA, et al. (2006) Sensitivity analysis of viscoelastic structures. *Shock and Vibration* 13: 545–558.

Friswell MI, Dutt JK, Adhikari S, et al. (2010) Time domain analysis of a viscoelastic rotor using internal variable models. *International Journal of Mechanical Sciences* 52(10): 1319–1324.

Genta G and Amati N (2010) Hysteretic damping in rotor dynamics: an equivalent formulation. *Journal of Sound and Vibration* 329(22): 4772–4784.

Genta G, Bassani D and Delprete C (1996) DYNROT: a finite element code for rotor dynamic analysis based on complex co-ordinates. *Engineering Computations* 13(6): 86–109.

Golla DF and Hughes PC (1985) Dynamics of viscoelastic structures: a time domain finite element formulation. *Journal of Applied Mechanics* 52: 897–906.

Hong SW and Park JH (1999) Dynamic analysis of multi-stepped distributed parameter rotor-bearing systems. *Journal of Sound and Vibration* 227(4): 769–785.

Kang CH, Hsu WC, Lee EK, et al. (2011) Dynamic analysis of gear-rotor system with viscoelastic supports under residual shaft bow effect. *Mechanism and Machine Theory* 46(3): 264–275.

Kliem W (1987) The dynamics of viscoelastic rotors. *Dynamics and Stability of Systems* 2(1): 424–429.

Lalanne M and Ferraris G (1998) *Rotor Dynamics Prediction in Engineering*. Chichester, UK: John Wiley and Sons Ltd.

Lara-Molina FA, Koroishi EH and Steffen V Jr. (2015) Uncertainty analysis of flexible rotors considering fuzzy parameters and fuzzy-random parameters. *Latin American Journal of Solids and Structures* 12: 1807–1823.

Lesieutre GA and Bianchini E (1995) Time domain modeling of linear viscoelasticity using anelastic displacement fields. *Journal of Vibration and Acoustics* 117: 424–430.

Lesieutre GA and Mingori DL (1990) Finite element modeling of frequency-dependent material damping using augmenting thermodynamic fields. *Journal of Guidance, Control and Dynamics* 13(6): 1040–1050.

Lesieutre GA, Bianchini E and Maiani A (1996) Finite element modeling of one-dimensional viscoelastic structures using anelastic displacement fields. *Journal of Guidance, Control and Dynamics* 19(3): 520–527.

McTavish DJ and Hughes PC (1993) Modeling of linear viscoelastic space structures. *Journal of Vibration and Acoustics* 115: 103–110.

Morais TS, Steffen V and Mahfoud J Jr. (2012) Control of the breathing mechanism of a cracked rotor by using electro-magnetic actuator: numerical study. *Latin American Journal of Solids and Structures* 9: 581–596.

Nelson HD (1980) A finite rotating shaft element using Timoshenko beam theory. *Journal of Mechanical Design* 102: 793–803.

Nelson HD and McVaugh JM (1976) The dynamics of rotor-bearing systems using finite elements. *Journal of Engineering for Industry* 98(2): 593–600.

Recktenwal GW (2007) *Numerical Methods with Matlab: Implementations and Applications*. Upper Saddle River, NJ: Prentice-Hall.

Roy H, Dutt JK and Chandraker S (2012) Modelling of multilayered viscoelastic rotors – an operator based approach. In: *8th international conference on vibration engineering and technology of machinery (VETOMAC VIII)*, Gdansk, Poland, 3–6 September 2012.

Roy H, Dutt JK and Datta PK (2009) Dynamics of multilayered viscoelastic beams. *Structural Engineering and Mechanics* 33(4): 391–406.

Rusovici R (1999) *Modeling of shock wave propagation and attenuation in viscoelastic structures*. PhD Thesis, Virginia Polytechnic Institute and State University, USA.

Shabaneh NH and Zu JW (2000a) Dynamic and stability analysis of rotor–shaft systems with viscoelastically supported bearings. *Transactions of the Canadian Society for Mechanical Engineering* 24(1): 179–189.

Shabaneh NH and Zu JW (2000b) Dynamic analysis of rotor–shaft systems with viscoelastically supported bearings. *Mechanism and Machine Theory* 35(9): 1313–1330.

Sinha SK (1989) Stability of a viscoelastic rotor-disk system under dynamic axial loads. *AIAA Journal* 27(11): 1653–1655.

Sturla FA and Argento A (1996) Free and forced vibrations of a spinning viscoelastic beam. *Journal of Vibration and Acoustics* 118(3): 463–468.

Timoshenko S (1940) *Strength of Materials – Part I*. New York: D Van Nostrand Co Inc.

Wagner N and Adhikari S (2003) Symmetric state-space formulation for a class of non-viscously damped systems. *AIAA Journal* 41: 951–956.

Walking Randomly (2013) Simple nonlinear least squares curve fitting in MATLAB. Available at: http://walkingrandomly.com/ (accessed 25 November 2014).

Williams ML (1964) Structural analysis of viscoelastic materials. *AIAA Journal* 2(5): 785–808.

Xiong GL, Yi JM, Zeng C, et al. (2003) Study of the gyroscopic effect of the spindle on the stability characteristics of the milling system. *Journal of Materials Processing Technology* 138: 379–384.

Appendix 1

The following matrices have been derived for a Timoshenko viscoelastic beam element with symmetrical cross section

$$I_y = I_z = I \quad \text{and} \quad \Phi_y = \Phi_z = \Phi = \frac{12EI}{\kappa AGl^2}$$

1. Element stiffness matrix: $\left[K_e^e\right] = \left[K_e^e\right]_o + \Phi\left[K_e^e\right]_1$, where

$$\left[K_e^e\right]_o = \frac{EI}{l^3(1+\Phi)} \begin{bmatrix} 12 & 0 & 0 & 6l & -12 & 0 & 0 & 6l \\ & 12 & 6l & 0 & 0 & -12 & -6l & 0 \\ & & 4l^2 & 0 & 0 & 6l & 2l^2 & 0 \\ & & & 4l^2 & -6l & 0 & 0 & 2l^2 \\ & & & & 12 & 0 & 0 & -6l \\ & & \text{sym} & & & 12 & 6l & 0 \\ & & & & & & 4l^2 & 0 \\ & & & & & & & 4l^2 \end{bmatrix}$$

$$\left[K_e^e\right]_1 = \frac{EI}{l^3(1+\Phi)}\begin{bmatrix} 0 & 0 & 0 & 0 & 0 & 0 & 0 & 0 \\ & 0 & 0 & 0 & 0 & 0 & 0 & 0 \\ & & l^2 & 0 & 0 & 0 & -l^2 & 0 \\ & & & l^2 & 0 & 0 & 0 & -l^2 \\ & & & & 0 & 0 & 0 & 0 \\ & & \text{sym} & & & 0 & 0 & 0 \\ & & & & & & l^2 & 0 \\ & & & & & & & l^2 \end{bmatrix}$$

2. Element stiffness matrix for parallel branches: $\left[K_{ei}^e\right] = \left[K_{ei}^e\right]_o + \Phi_i\left[K_{ei}^e\right]_1$, where $\Phi = \frac{12E_iI}{\kappa AG_il^2}$ and $i = 1,\ 2,\ 3$

$$\left[K_{ei}^e\right]_o = \frac{E_iI}{l^3(1+\Phi_i)}\begin{bmatrix} 12 & 0 & 0 & 6l & -12 & 0 & 0 & 6l \\ & 12 & 6l & 0 & 0 & -12 & -6l & 0 \\ & & 4l^2 & 0 & 0 & 6l & 2l^2 & 0 \\ & & & 4l^2 & -6l & 0 & 0 & 2l^2 \\ & & & & 12 & 0 & 0 & -6l \\ & & \text{sym} & & & 12 & 6l & 0 \\ & & & & & & 4l^2 & 0 \\ & & & & & & & 4l^2 \end{bmatrix}$$

$$\left[K_{ei}^e\right]_1 = \frac{E_iI}{l^3(1+\Phi_i)}\begin{bmatrix} 0 & 0 & 0 & 0 & 0 & 0 & 0 & 0 \\ & 0 & 0 & 0 & 0 & 0 & 0 & 0 \\ & & l^2 & 0 & 0 & 0 & -l^2 & 0 \\ & & & l^2 & 0 & 0 & 0 & -l^2 \\ & & & & 0 & 0 & 0 & 0 \\ & & \text{sym} & & & 0 & 0 & 0 \\ & & & & & & l^2 & 0 \\ & & & & & & & l^2 \end{bmatrix}$$

3. Element damping matrix for parallel branches: $\left[K_{bi}^e\right] = \left[K_{bi}^e\right]_o + \Phi_\eta i\left[K_{bi}^e\right]_1$, where $\Phi_\eta i = \frac{12\eta_{\varepsilon i}I}{\kappa A\eta_{\gamma i}l^2}$ and $i = 1,\ 2,\ 3$

$$\left[K_{bi}^e\right]_o = \frac{\eta_{\varepsilon i}I}{l^3(1+\Phi_\eta i)}\begin{bmatrix} 12 & 0 & 0 & 6l & -12 & 0 & 0 & 6l \\ & 12 & 6l & 0 & 0 & -12 & -6l & 0 \\ & & 4l^2 & 0 & 0 & 6l & 2l^2 & 0 \\ & & & 4l^2 & -6l & 0 & 0 & 2l^2 \\ & & & & 12 & 0 & 0 & -6l \\ & & \text{sym} & & & 12 & 6l & 0 \\ & & & & & & 4l^2 & 0 \\ & & & & & & & 4l^2 \end{bmatrix}$$

$$\left[K_{bi}^{e}\right]_1 = \frac{\eta_{\varepsilon i} I}{l^3(1+\Phi_\eta \mathrm{i})} \begin{bmatrix} 0 & 0 & 0 & 0 & 0 & 0 & 0 & 0 \\ & 0 & 0 & 0 & 0 & 0 & 0 & 0 \\ & & l^2 & 0 & 0 & 0 & -l^2 & 0 \\ & & & l^2 & 0 & 0 & 0 & -l^2 \\ & & & & 0 & 0 & 0 & 0 \\ & & \text{sym} & & & 0 & 0 & 0 \\ & & & & & & l^2 & 0 \\ & & & & & & & l^2 \end{bmatrix}$$

7. Element translational mass matrix: $\left[M_T^e\right] = \left[M_T^e\right]_o + \Phi\left[M_T^e\right]_1 + \Phi^2\left[M_T^e\right]_2$, where

$$\left[M_T^e\right]_o = \frac{ml}{420(1+\Phi)^2} \begin{bmatrix} 156 & 0 & 0 & 22l & 54 & 0 & 0 & -13l \\ & 156 & -22l & 0 & 0 & 54 & 13l & 0 \\ & & 4l^2 & 0 & 0 & -12l & -3l^2 & 0 \\ & & & 4l^2 & 13l & 0 & 0 & -3l^2 \\ & & & & 156 & 0 & 0 & -22l \\ & & \text{sym} & & & 156 & 22l & 0 \\ & & & & & & 4l^2 & 0 \\ & & & & & & & 4l^2 \end{bmatrix}$$

$$\left[M_T^e\right]_1 = \frac{ml}{420(1+\Phi)^2} \begin{bmatrix} 294 & 0 & 0 & 38.5l & 126 & 0 & 0 & -31.5l \\ & 294 & -38.5l & 0 & 0 & 126 & 31.5l & 0 \\ & & 7l^2 & 0 & 0 & -31.5l & -7l^2 & 0 \\ & & & 7l^2 & 31.5l & 0 & 0 & -7l^2 \\ & & & & 294 & 0 & 0 & -38.5l \\ & & \text{sym} & & & 294 & 38.5l & 0 \\ & & & & & & 7l^2 & 0 \\ & & & & & & & 7l^2 \end{bmatrix}$$

$$\left[M_T^e\right]_2 = \frac{ml}{420(1+\Phi)^2} \begin{bmatrix} 140 & 0 & 0 & 17.5l & 70 & 0 & 0 & -17.5l \\ & 140 & -17.5l & 0 & 0 & 70 & 17.5l & 0 \\ & & 3.5l^2 & 0 & 0 & -17.5l & -3.5l^2 & 0 \\ & & & 3.5l^2 & 17.5l & 0 & 0 & -3.5l^2 \\ & & & & 140 & 0 & 0 & -17.5l \\ & & \text{sym} & & & 140 & 17.5l & 0 \\ & & & & & & 3.5l^2 & 0 \\ & & & & & & & 3.5l^2 \end{bmatrix}$$

8. Element rotational mass matrix: $\left[M_R^e\right] = \left[M_R^e\right]_o + \Phi\left[M_R^e\right]_1 + \Phi^2\left[M_R^e\right]_2$, where

$$\left[M_R^e\right]_o = \frac{mr^2}{120l(1+\Phi)^2} \begin{bmatrix} 36 & 0 & 0 & 3l & -36 & 0 & 0 & 3l \\ & 36 & -3l & 0 & 0 & -36 & -3l & 0 \\ & & 4l^2 & 0 & 0 & 3l & -l^2 & 0 \\ & & & 4l^2 & -3l & 0 & 0 & -l^2 \\ & & & & 36 & 0 & 0 & -3l \\ & & \text{sym} & & & 36 & 3l & 0 \\ & & & & & & 4l^2 & 0 \\ & & & & & & & 4l^2 \end{bmatrix}$$

$$[M_R^e]_1 = \frac{mr^2}{120l(1+\Phi)^2}\begin{bmatrix} 0 & 0 & 0 & -15l & 0 & 0 & 0 & -15l \\ & 0 & 15l & 0 & 0 & 0 & 15l & 0 \\ & & 5l^2 & 0 & 0 & -15l & -5l^2 & 0 \\ & & & 5l^2 & 15l & 0 & 0 & -5l^2 \\ & & & & 0 & 0 & 5l^2 & 15l \\ & & \text{sym} & & & 0 & -15l & 0 \\ & & & & & & 5l^2 & 0 \\ & & & & & & & 5l^2 \end{bmatrix}$$

$$[M_R^e]_2 = \frac{mr^2}{120l(1+\Phi)^2}\begin{bmatrix} 0 & 0 & 0 & 0 & 0 & 0 & 0 & 0 \\ & 0 & 0 & 0 & 0 & 0 & 0 & 0 \\ & & 10l^2 & 0 & 0 & 0 & 5l^2 & 0 \\ & & & 10l^2 & 0 & 0 & 0 & 5l^2 \\ & & & & 0 & 0 & 0 & 0 \\ & & \text{sym} & & & 0 & 0 & 0 \\ & & & & & & 10l^2 & 0 \\ & & & & & & & 10l^2 \end{bmatrix}$$

9. Element gyroscopic mass matrix: $[G^e] = 2[\hat{M}_T^e] = \frac{2}{\omega}[R]^T[M_T^e][\dot{R}]$, where $[R]$ is the orthogonal transformation matrix between the inertia and spinning frames. Therefore, $[G^e] = [G^e]_o + \Phi[G^e]_1 + \Phi^2[G^e]_2$, where

$$[G^e]_o = \frac{ml}{420(1+\Phi)^2}\begin{bmatrix} 0 & -156 & -22l & 0 & 0 & -54 & -13l & 0 \\ & 0 & 0 & 22l & 54 & 0 & 0 & -13l \\ & & 0 & -4l^2 & -13l & 0 & 0 & 3l^2 \\ & & & 0 & 0 & -13l & -3l^2 & 0 \\ & & & & 0 & -156 & -22l & 0 \\ & \text{skew} & \text{sym} & & & 0 & 0 & -22l \\ & & & & & & 0 & -4l^2 \\ & & & & & & & 0 \end{bmatrix}$$

$$[G^e]_1 = \frac{ml}{420(1+\Phi)^2}\begin{bmatrix} 0 & -294 & -38.5l & 0 & 0 & -126 & -31.5l & 0 \\ & 0 & 0 & 38.5l & -126 & 0 & 0 & -31.5l \\ & & 0 & -7l^2 & -31.5l & 0 & 0 & -7l^2 \\ & & & 0 & 0 & -31.5l & -7l^2 & 0 \\ & & & & 0 & -294 & -38.5l & 0 \\ & \text{skew} & \text{sym} & & & 0 & 0 & -38.5l \\ & & & & & & 0 & -7l^2 \\ & & & & & & & 0 \end{bmatrix}$$

$$[G^e]_2 = \frac{ml}{420(1+\Phi)^2}\begin{bmatrix} 0 & -140 & -17.5l & 0 & 0 & -70 & -17.5l & 0 \\ & 0 & 0 & 17.5l & 70 & 0 & 0 & -17.5l \\ & & 0 & -3.5l^2 & -17.5l & 0 & 0 & 3.5l^2 \\ & & & 0 & 0 & -17.5l & -3.5l^2 & 0 \\ & & & & 0 & -140 & -17.5l & 0 \\ & \text{skew} & \text{sym} & & & 0 & 0 & -17.5l \\ & & & & & & 0 & -3.5l^2 \\ & & & & & & & 0 \end{bmatrix}$$